Publications of the Astronomical Society of the Pacific
**108:** 510–519, 1996 June

# Searching for Faint Companions to Nearby Stars with the *Hubble Space Telescope*

DANIEL J. SCHROEDER

Department of Physics and Astronomy, Beloit College, Beloit, Wisconsin 53511
Electronic mail: schroeder@beloit.edu

DAVID A. GOLIMOWSKI

Center for Astrophysical Sciences, Department of Physics and Astronomy, The Johns Hopkins University,
Baltimore, Maryland 21218
Electronic mail: dag@pha.jhu.edu

*Received 1996 February 2; accepted 1996 April 3*

**ABSTRACT.** A search for faint companions (FCs) to selected stars within 5 pc of the Sun using the *Hubble Space Telescope*'s Planetary Camera (PC) has been initiated. To assess the PC's ability to detect FCs, we have constructed both model and laboratory-simulated images and compared them to actual PC images. We find that the PC's point-spread function (PSF) is 3–4 times brighter over the angular range 2″–5″ than the PSF expected for a perfect optical system. Azimuthal variations of the PC's PSF are 10–20 times larger than expected for a perfect PSF. These variations suggest that light is scattered nonuniformly from the surface of the detector. Because the anomalies in the PC's PSF cannot be precisely simulated, subtracting a reference PSF from the PC image is problematic. We have developed a computer algorithm that identifies local brightness anomalies within the PSF as potential FCs. We find that this search algorithm will successfully locate FCs anywhere within the circumstellar field provided that the average pixel signal from the FC is at least $10\sigma$ above the local background. This detection limit suggests that a comprehensive search for extrasolar Jovian planets with the PC is impractical. However, the PC is useful for detecting other types of substellar objects. With a stellar signal of $10^9\ e^-$, for example, we may detect brown dwarfs as faint as $M_I = 16.7$ separated by 1″ from $\alpha$ Cen A.

## 1. INTRODUCTION

Obtaining direct images of faint companions (FCs) to bright stars is a difficult enterprise with any telescope, even the repaired *Hubble Space Telescope* (*HST*). Since the present complement of cameras aboard *HST* lacks a coronagraphic mode, the background above which a FC must be detected is determined by the primary star's point-spread function (PSF) and by light scattered from the telescope and camera optics. Whether the FC is a very-low-mass star, a brown dwarf, or a giant planet, its detectability in the presence of this background depends on its brightness relative to the primary star, its angular distance from the primary star, and the structure of the primary star's PSF.

A search for extrasolar planets using *HST*'s Planetary Camera (PC) was first proposed by Fastie et al. (1985). Assuming a perfect instrumental PSF and a planet-to-star flux ratio of $10^{-8}$, they determined that a $3\sigma$ detection of a planet was possible if the planet were located in the interference minima of a narrow-band star image. Using prelaunch metrology data to derive *HST*'s PSF, Brown and Burrows (1990) concluded that the flux ratio between a planet and the local stellar background would be unfavorable for planet detection even under the most optimistic viewing circumstances. The subsequent discovery of spherical aberration in *HST*'s primary mirror precluded any empirical assessment of *HST*'s ability to detect FCs. Now that the intrinsic imaging capability of *HST* has been restored, such an assessment can be performed.

A search for FCs to selected stars within 5 pc of the Sun has been initiated by *HST* Guaranteed Time Observers W. G. Fastie and D. J. Schroeder using the PC mode of the Wide Field and Planetary Camera 2 (WFPC2). Originally intended to commence after the launch of *HST* in 1990, this program was postponed until the repair of the telescope was completed in early 1994. The target stars have visual magnitudes ranging from −1 to +13, and so permit an analysis of FC detectability over a wide range of background levels.

This paper comprises three main parts. First, we characterize the PSF of the PC by comparing actual PC images to laboratory-generated images and to model images computed for an aberration-free *HST*+PC pupil. Second, we describe an algorithm for finding FCs superposed on the wings of the PSF. We apply this search algorithm to noisy model images of binary systems and establish a minimum signal limit for detecting FCs. Finally, we use this signal limit to assess the feasibility of detecting extrasolar planets and other substellar objects with the PC.

## 2. PSF CHARACTERISTICS

The number of photons required for the detection of a FC at a given distance from its primary star is governed by the brightness of the local background, the saturation level of the detector, and the desired level of signal to noise (S/N). For

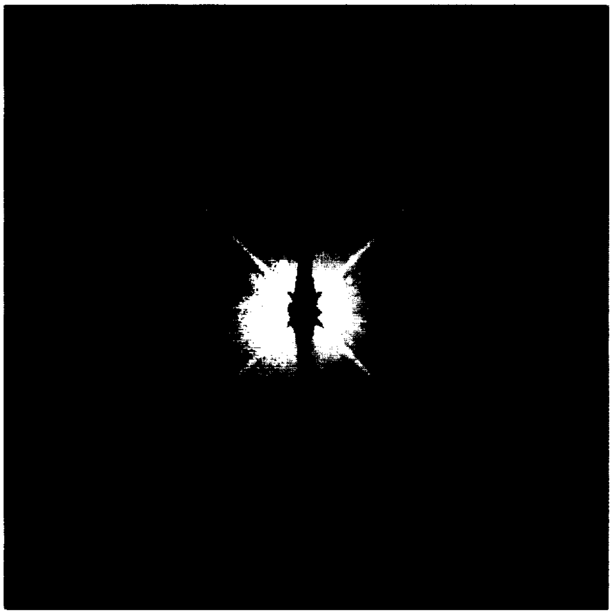

FIG. 1—Median of 56 images of a star obtained with *HST*'s Planetary Camera and the F555W filter (WFPC2 *V*). The logarithm of the data is shown to reduce image contrast. The figure shows the 27″×27″ section of the full CCD frame centered on the star. The total detected signal per exposure is $1.2\times10^9\ e^-$. The blackened region depicts the area of detector saturation. Note the radial streamers emanating from the center of the PSF. A faint background star can be seen at the extreme left of the image.

many of our target stars, we selected individual CCD exposure times that produced a total detected signal of $\sim10^9\ e^-$. At this signal level, the saturated core of the PSF extends outward to a radius of ~1″.

Figure 1 shows a median PC image of a star exposed to a level of $1.2\times10^9\ e^-$ through the F555W (WFPC2 *V*) filter. The image is a 27″×27″ section of the full CCD frame centered on the star. The PSF is clearly not smooth. The diffraction spikes caused by the secondary-mirror supports and the charge overflow from the saturated CCD pixels (charge "bleed") are prominent. Also apparent are several radial "streamers" emanating from the center of the PSF. The structure of the PSF is more easily seen in Fig. 2, which shows a surface plot of a 9″×9″ region at the left center of Fig. 1. Again, the diffraction spikes and the plateau of saturated pixels are obvious. More evident are the radial streamers, which decay gradually to the level of the detector noise.

To understand the complicated nature of the PC's PSF, an analysis of both theoretical and optically simulated PSFs is required. Consequently, we now discuss the formation and analysis of model and laboratory-generated PSFs. Afterward, we will return to the detailed examination of the PC images.

## 2.1 Model PSFs

The PSF for the aberration-free *HST*+PC pupil can be computed using the procedure and notation of Schroeder (1987). The complex amplitude of the wave front $U(P)$ at point $P$ in the focal plane is

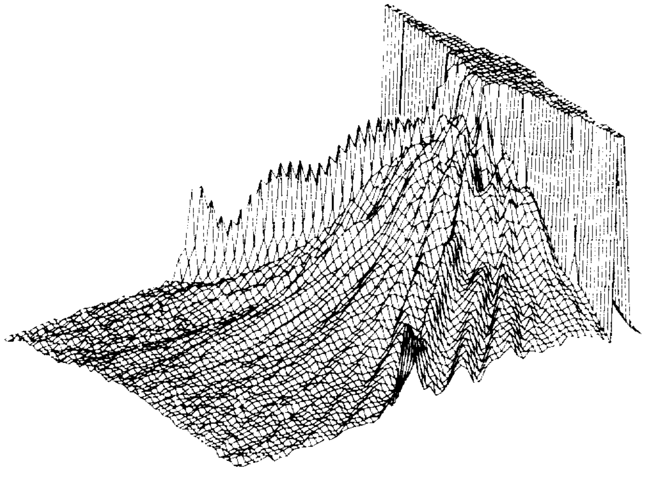

FIG. 2—Surface plot of the 9″×9″ region at the left center of Fig. 1, viewed along the lower-left diffraction spike. The pixels have been block averaged in 3×3 bins for clarity.

$$\begin{aligned} U(P)=C\Bigg\{&\pi R^2\left[\frac{2J_1(\eta)}{\eta}-\varepsilon^2\,\frac{2J_1(\varepsilon\eta)}{\varepsilon\eta}\right] \\ &-\pi\rho^2\,\frac{2J_1(\delta)}{\delta}\sum_{m=1}^{3}\exp[-iK(X_m u+Y_m v)] \\ &-2bd\left[\cos(KSu)\,\mathrm{sinc}\left(\frac{Kbv}{2}\right)\mathrm{sinc}\left(\frac{Kdu}{2}\right)\right. \\ &\left.+\cos(KSv)\,\mathrm{sinc}\left(\frac{Kbu}{2}\right)\mathrm{sinc}\left(\frac{Kdv}{2}\right)\right]\Bigg\}, \end{aligned} \tag{1}$$

where $R$ is the radius of the *HST* primary mirror; $\rho$ is the radius of a primary-mirror support pad; $b$ is the width of the secondary-mirror support ("spider leg"); $d$ is the length of the spider leg; $\varepsilon$ is the secondary-mirror obscuration ratio; $K=2\pi/\lambda f$, where $f$ is the effective focal length; $X_m$ and $Y_m$ are the Cartesian coordinates of the $m$th pad; $u$ and $v$ are the Cartesian coordinates of $P$; $\eta=KR(u^2+v^2)^{1/2}$; $\delta=K\rho(u^2+v^2)^{1/2}$; and $S=R(1+\varepsilon)/2$ is the distance between the geometric centers of a spider leg and the secondary mirror.

The constant $C$ is chosen so that $U^*U=1$ at the image center ($u=v=\eta=0$), i.e.,

$$C^2(\pi R^2)^2\left[(1-\varepsilon^2)-\frac{4bd}{\pi R^2}-3\left(\frac{\rho}{R}\right)^2\right]^2=1. \tag{2}$$

The first two terms in Eq. (1) represent the annular pupil created by the PC secondary-mirror obscuration. The third term describes the obscuration by the three *HST* primary-mirror support pads. The final two terms describe the *HST*+PC spider. The pupil represented by Eq. (1) is shown in Fig. 3.

When projected onto the plane of the *HST* pupil, the central obscuration and spider from the PC reimaging optics are larger than those of the intrinsic *HST* pupil. The PC spider has only three legs, however, so one narrow leg of the *HST* spider remains visible in the composite pupil. We did not include this width difference in Eq. (1) because, as we later

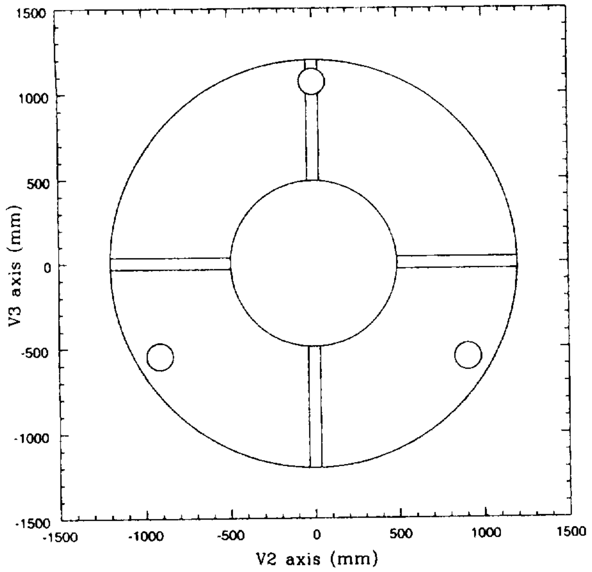

FIG. 3—The model pupil described by Eq. (1) with the following dimensions (Krist 1994): $R=1200$ mm, $\rho=78$ mm, $b=69.6$ mm, $d=708$ mm, $\varepsilon=0.41$, $f=28.3$, $(X_1,Y_1)=(0,1070.5)$ mm, $(X_2,Y_2)=(906.6,-553.8)$ mm, and $(X_3,Y_3)=(-912.7,-547.7)$ mm. The coordinates of the optical components are measured relative to the V2 and V3 spacecraft axes. The pupil shown differs from the *HST*+PC pupil only in the thickness of the +V3 spider leg. The actual width of the +V3 leg is 25.7 mm. The effect of this difference on the resulting PSF is negligible compared to the larger differences noted between the model and actual PSFs.

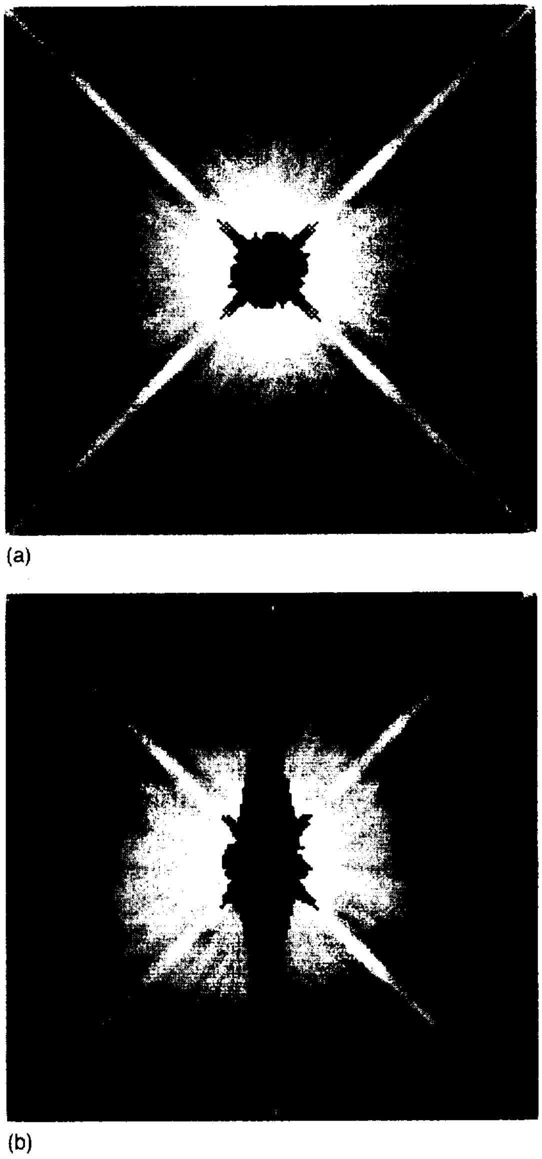

FIG. 4—(a) Model PSF computed for F555W filter. The logarithm of the data is shown to reduce image contrast. The field of view is 9″×9″. The blackened region depicts the extent of detector saturation (pixel signal $>5.3\times10^4$ $e^-$) for an exposure level of $10^9$ $e^-$. (b) The central 9″×9″ region of the real F555W image shown in Fig. 1. Again, the blackened region depicts the area of detector saturation. Note the enhanced surface brightness of the real image beyond the saturated region.

show, its effect on the resulting PSF is negligible compared to the large overall differences between the real and model PSFs.

Using Eq. (1), we created model PSFs for several broadband filters available with the PC. Each polychromatic PSF was formed by summing 25–50 monochromatic PSFs, each separately computed and scaled in proportion to the overall system response at that wavelength (Burrows et al. 1995). Figure 4(a) shows the central 9″×9″ region of a model PSF computed for the F555W filter, and Fig. 4(b) shows the same region of the real F555W image seen in Fig. 1. The average signal per pixel in the wings of the model PSF, $\langle I\rangle$, is given by

$$\frac{\langle I\rangle}{E}=6.9\times10^{-6}\left(\frac{\langle\lambda\rangle_{\rm nm}}{550}\right)\alpha^{-3}, \qquad (3)$$

where $E$ is the total signal in the PSF, $\langle\lambda\rangle_{\rm nm}$ is the mean wavelength of the bandpass in nanometers, and $\alpha$ is the angular distance in arcseconds from the PSF center. Equation (3), with $E=10^9$ $e^-$, serves as the reference against which real PC images will be compared.

If the terms representing the support pads and spider are omitted from Eq. (1), then $\langle I\rangle/E$ is reduced by 25%. This reduction is almost entirely due to the pads, which cover about 0.0146 of the pupil area and have diameters ~16 times smaller than the *HST* aperture. According to diffraction theory, the pads should raise $\langle I\rangle/E$ in the wings of the PSF by an amount equal to the product of these factors, or about 0.23. Thus, the spider contributes about 2% of the average surface brightness of the PSF. The symmetric-spider approximation used in Eq. (1) will not, therefore, significantly effect the accuracy of the model PSFs.

## 2.2 Laboratory-Generated PSFs

Before the launch of *HST* in 1990, a laboratory simulator (SIM) was constructed to reproduce the images obtained with the original Wide Field/Planetary Camera (WF/PC). With SIM, the scattered light associated with heavily saturated WF/PC images could be directly measured, and the feasibility of imaging Jovian planets around nearby stars could be assessed. Following the decision to replace WF/PC with WFPC2, SIM was modified in accordance with the proposed changes to the PC.

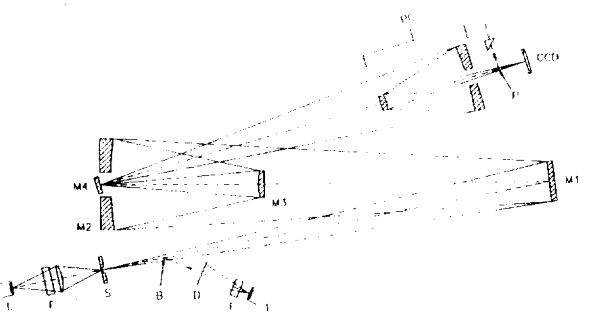

FIG. 5—Schematic of the laboratory *HST*+PC simulator (SIM) at The Johns Hopkins University. Legend: D, diffuser; F, filter; L, lamp; M, mirror; P, periscope; S, pinhole source.

A schematic of the modified SIM is shown in Fig. 5. Light from a halogen lamp (*L*) illuminates a 5-$\mu$m-diameter pinhole (S) through a filter (F). A flat mirror (M1) directs this simulated-star light into a Dall–Kirkham reimager (M2 +M3) whose entrance aperture is 1/32 that of *HST*. This reimager produces an $f/24$ output beam like that of *HST*. A concave spherical mirror (M4), located at the $f/24$ focus, images the Dall–Kirkham pupil onto the secondary mirror of a flight-qualified spare PC provided by NASA's Jet Propulsion Laboratory. The PC then reimages the simulated star at $f/28.3$ onto a flight-spare Loral 800×800 pixel frontside-illuminated CCD. By inserting a diffusely illuminated screen (D) into the optical path at point B, flat-field calibration images may be obtained for each filter. A periscope (P) permits visual inspection of either the exit pupil or the image during optical alignment.

The diameter of the PC's Airy diffraction disk is 22 $\mu$m at $\lambda=633$ nm. Because the Dall–Kirkham reimager produces a geometric image of S that is twice diminished, the use of a 5-$\mu$m-diameter pinhole as a simulated-star source has a negligible effect on the shape of the instrumental PSF. Moreover, the geometric-image size of $\alpha$ Centauri A at the $f/24$ *HST* focal plane is 3 $\mu$m, which is comparable to the 2.5 $\mu$m geometric-image size of the pinhole source.

We assessed the overall image quality of SIM by comparing the observed narrow-band image sharpness to that expected for a perfect detector and optics of varying surface quality. Following the example of Hasan (1994), we define sharpness as

$$S=\sum_i P_i^2 \Bigg/ \left(\sum_j P_j\right)^2, \tag{4}$$

where $P_i$ is the signal of the $i$th pixel lying within an $n\times n$ pixel array centered on the simulated-star image. Good sensitivity to focus was found using $n=7$ in the numerator and $n=11$ in the denominator. Using a narrow-band F889N filter ($\langle\lambda\rangle=889$ nm, $\Delta\lambda=52$ nm), best focus was found when $S=0.027$. Similar analyses of F889N images obtained with a flight-spare WF/PC detector (a TI 800×800 pixel backside-illuminated CCD) in place of the WFPC2 detector gave $S=0.034$ at best focus. The disparity in sharpness between detectors is likely due to the unfavorable pixel-response function of the Loral CCD (Burrows et al. 1995). The latter value, $S=0.034$, is equivalent to a rms wave-front error of $\sim\lambda/6$ at $\lambda=633$ nm. Thus, the rms surface quality of the SIM optics is $\sim\lambda/12$ or better.

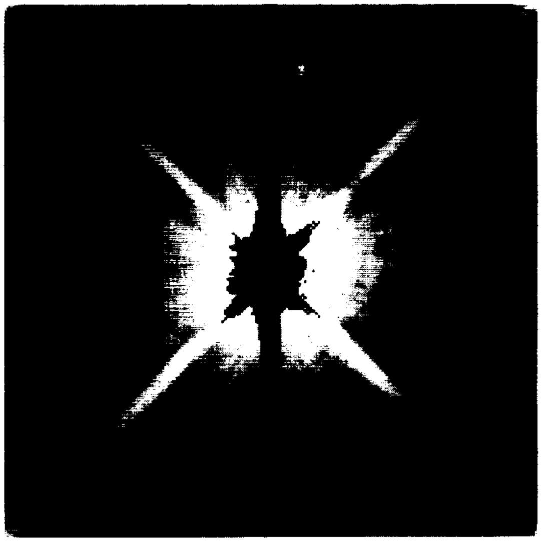

FIG. 6—SIM image through F555W filter exposed to a level of ~$10^9$ $e^-$. The logarithm of the data is shown to reduce image contrast. The field of view is 9″×9″. The blackened region depicts the extent of detector saturation. Radial streamers like those seen in the equivalent *HST* image [Fig. 4(b)] are clearly evident. The bright spots and halo of radius ~4″ centered roughly on the simulated star are reflections from an optical surface within SIM's PC section.

Figure 6 shows the central 9″×9″ region of a SIM image through the F555W filter exposed to a level of ~$10^9$ $e^-$. This image may be compared directly to the equivalent model and *HST* images shown in Fig. 4. Radial streamers like those seen in the *HST* image are clearly evident. The bright spots and halo of radius ~4″ centered roughly on the simulated star are caused by reflections within SIM's PC section.

### 2.3 Comparison of PSF Results

To understand the structure of the PC images represented by Fig. 1, we first measured the azimuthal variations of the PSF at selected values of $\alpha$. We computed the average pixel signals within 5×5 pixel boxes located at 30° intervals along concentric circles with $\alpha=2'',3'',\ldots,10''$. (The size of the boxes was chosen arbitrarily.) Care was taken to avoid regions of CCD saturation and the diffraction spikes caused by the pupil spider. Figure 7 shows the azimuthal brightness variations for the image shown in Fig. 1. The brightness varies by factors of 2–3 along any given circle. Azimuthal plots obtained for images taken through other filters or at different locations on the CCD show similar variability.

The images obtained with SIM show azimuthal variations similar to those of the PC images. Along a given circle, the brightness of the SIM images varies by a factor of ~2. By contrast, the azimuthal variations of the model PSFs described by Eq. (1) are about 10%. This difference between the actual and theoretical PSFs suggests that light is scattered radially but nonuniformly from the surface of the CCD and then reflected back onto the CCD by other surfaces within the PC. Krist (1995) has reached the same conclusion by

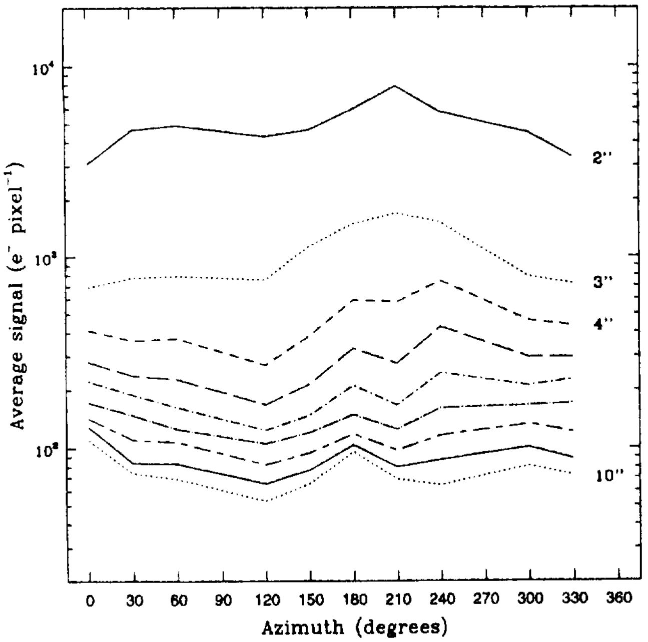

FIG. 7—Azimuthal brightness variations of the PSF shown in Fig. 1. The curves connect points reflecting the average signal within a 5×5 pixel box located at 30° intervals along concentric circles of radius 2″,3″,...,10″. Data along the azimuths of the charge bleed and spider diffraction spikes have been excluded.

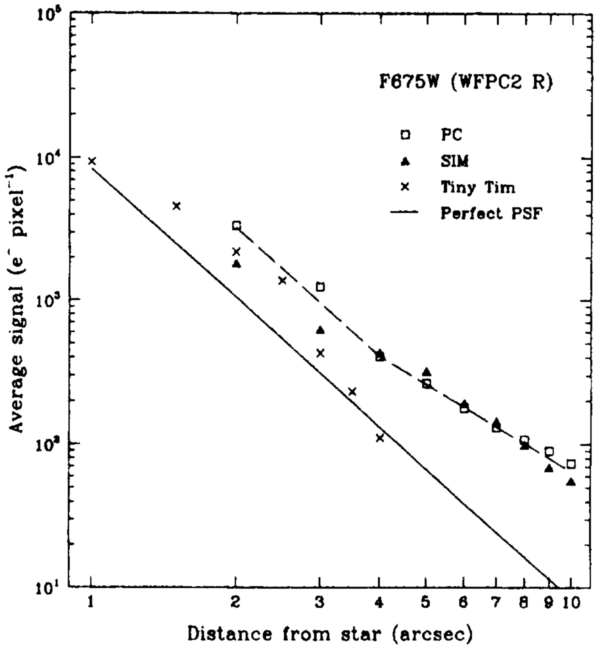

FIG. 9—Average radial profile of PC's PSF through the F675W (WFPC2 *R*; $\langle\lambda\rangle = 669.6$ nm, $\Delta\lambda = 86.6$ nm) filter. All symbols are defined in Fig. 8. The dashed line through the PC data has slope $-3$ for $\alpha < 4''$ and slope $-2$ for $\alpha > 4''$.

comparing the levels of large-angle scattered light in adjoining WFPC2 CCDs.

To investigate the bandpass dependence of the PC, SIM, and model PSFs, we azimuthally averaged the brightness profiles computed for each of several WFPC2 filters. We thus obtained an average radial profile sampled at successive 1″ intervals for each bandpass. Figures 8–11 show the radial profiles for the F555W, F675W, F814W, and F850LP filters, respectively. Each figure displays the data obtained from actual PC images, SIM images, and images computed using the *HST* PSF modeling program Tiny Tim (Krist 1994). All images were normalized to a total signal of $10^9$ $e^-$. Also plotted in each figure is a line of slope $-3$, which represents the radial power-law index of the perfect PSF given by Eq. (3) with $E = 10^9$ $e^-$.

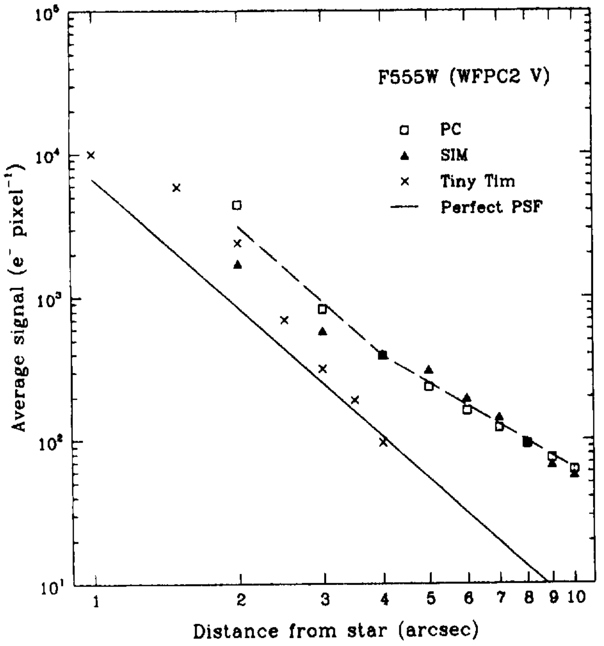

FIG. 8—Average radial profile of PC's PSF through the F555W (WFPC2 *V*; $\langle\lambda\rangle = 539.8$ nm, $\Delta\lambda = 122.6$ nm) filter. Data are shown for actual PC images (*open squares*), SIM images (*filled triangles*), and Tiny Tim models (Krist 1994) (*crosses*). The solid line of slope $-3$ represents the profile of the perfect image given by Eq. (3). The dashed line through the PC data has slope $-3$ for $\alpha < 4''$ and slope $-2$ for $\alpha > 4''$.

Figures 8–11 show that the actual PC profiles are 3–4 times brighter than the perfect profiles in the range $2'' < \alpha < 4''$ ($2'' < \alpha < 5''$ for the redder bandpasses), but retain the $-3$ slope characteristic of a perfect PSF. Beyond this range, the slope of the PC profiles changes to approximately $-2$. On the other hand, the SIM profiles are 1.5–2 times brighter than the perfect profiles within 3″ and over 4 times brighter beyond 5″. The SIM profiles match well the PC profiles in the range $5'' < \alpha < 7''$, but are up to 2 times fainter within 3″ and beyond 8″. We estimate that the PC and SIM data are photometrically accurate to ±10%.

The differences between the PC and SIM image profiles are probably due to one or both of the following: (1) *HST*'s mirrors have zonal figure errors incurred during polishing, whereas SIM's small mirrors are unlikely to have such errors; and (2) the PC has a $MgF_2$ field-flattening lens close to the CCD, whereas SIM has no such lens. Krist and Burrows (1995) have produced accurate zonal-error maps of *HST*'s mirrors from their phase-retrieval analysis of WFPC2 images. These maps have been incorporated into Tiny Tim (Krist 1994). Figures 8–11 show that the Tiny Tim image profiles are brighter than the SIM profiles in the range

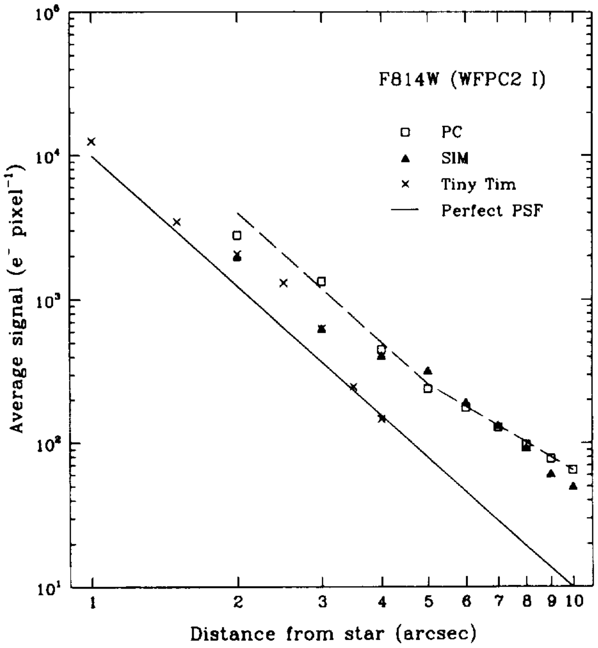

FIG. 10—Average radial profile of PC's PSF through the F814W (WFPC2 *I*; $\langle\lambda\rangle=792.1$ nm, $\Delta\lambda=148.9$ nm) filter. All symbols are defined in Fig. 8. The dashed line through the PC data has slope $-3$ for $\alpha<5''$ and slope $-2$ for $\alpha>5''$.

$1''<\alpha<3''$, but are fainter than the actual PC images within this range. Thus it is likely that the zonal errors in the *HST* optics are at least partly responsible for the discrepancies between the PC and SIM profiles. It is unclear from our analysis whether the field-flattening lens has any significant effect on the PSF.

In summary, we find that (1) the PC's PSF at $\alpha>2''$ has an average surface brightness that is significantly higher than expected with a perfect detector and optics, and (2) the azimuthal variations of the PC's PSF are substantially greater than those of a perfect system. These two conclusions strongly influence our approach to searching for FCs.

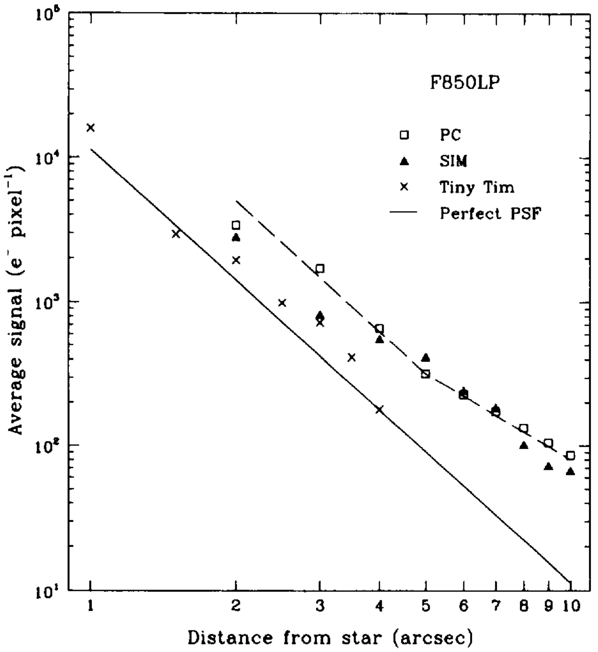

FIG. 11—Average radial profile of PC's PSF through the F850LP ($\langle\lambda\rangle=907.2$ nm, $\Delta\lambda=98.6$ nm) filter. All symbols are defined in Fig. 8. The dashed line through the PC data has slope $-3$ for $\alpha<5''$ and slope $-2$ for $\alpha>5''$.

## 3. FAINT-COMPANION SEARCH STRATEGY

The results of the previous section exclude conventional means of identifying FCs within the PSFs of bright stars. The gross differences between the PC images and both the model and SIM images prevent the use of the latter two as reference images for PSF subtraction. Furthermore, the use of non-target-star images as PSF references is plagued with practical difficulties. First, there is no guarantee that such a reference star lacks circumstellar emission at a detectable level. Second, a reference star of identical spectral class and angular size must be observed to prevent filter- or size-induced differences between the target and reference PSFs. Because our target stars lie within 5 pc of the Sun, it is nearly impossible to find a reference star that satisfies both requirements. Any such star would likely be a target star itself. Finally, Krist (1995) has noted that the radial streamers in an overexposed image vary with position on the CCD. To ensure a good match between the target and reference PSFs, interactive acquisition of the reference star is required. This interaction with *HST* would greatly diminish the efficiency of the observing program.

Given the intrinsic difficulties associated with PSF subtraction, we have adopted a strategy of examining local brightness anomalies within the target-star's PSF for possible FCs. We have devised a search algorithm that compares the signal of each image pixel with the local-average pixel signal. By median combining several images of the target field, cosmic-ray hits and other transient artifacts are discarded from the analysis. The fine-lock pointing stability of *HST* (0.″004 rms≈0.1 PC pixel) ensures good registration of the images before median combining.

### 3.1 The Search Algorithm

The basic steps of the search algorithm are the following:

(1) Compute the average (or median) pixel signal, $\langle I\rangle$ in $e^-$, for all contiguous 5×5 arrays of image pixels.

(2) For each 5×5 array, calculate the Poisson noise, $\sigma=\sqrt{\langle I\rangle/M}$, where $M$ is the number of images used to produce the median image.

(3) Identify those arrays having at least one pixel whose signal deviates by $N\sigma$ from $\langle I\rangle$ according to

If $(I-\langle I\rangle)>N\sigma$, then FLAG=1 else FLAG=0.

(4) Generate a binary map of the 5×5 pixel arrays whose elements equal FLAG.

For a 600×600 pixel image, this algorithm produces a 120×120 element map of black (FLAG=0) and white (FLAG=1) elements. A visual display of this map shows clearly those areas of the PC image that have pixels significantly brighter than the local average. These areas of the PC

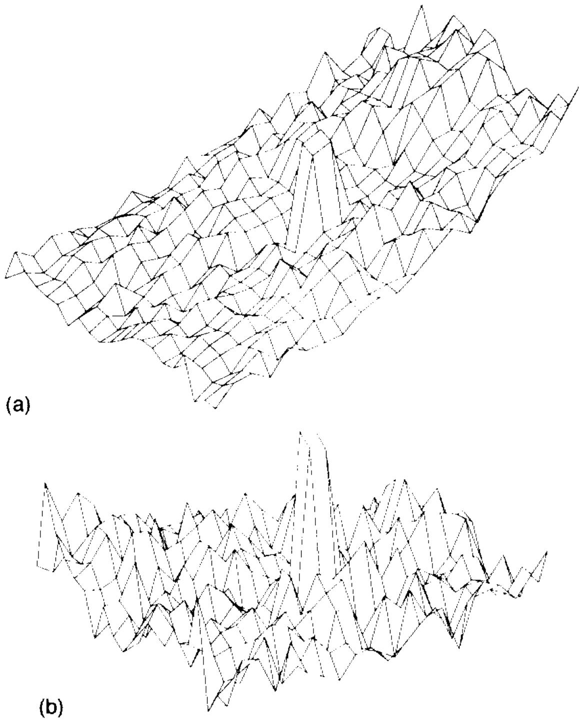

FIG. 12—Surface plots of a model F555W image containing a simulated companion located at $\alpha=4''$. The plots show the $1''\times 1''$ region of the primary star's PSF centered on the companion. The PSF has been scaled to give a total signal of $10^{10}\,e^{-}$. The companion's signal is divided uniformly over a $2\times 2$ pixel area so that each pixel is 10 $\sigma$ above the background. A Gaussian noise distribution has been added to mimic actual background fluctuations. (a) The region before removal of the PSF brightness gradient. (b) The region after removal of the gradient. The companion is clearly more noticeable in the background-flattened image.

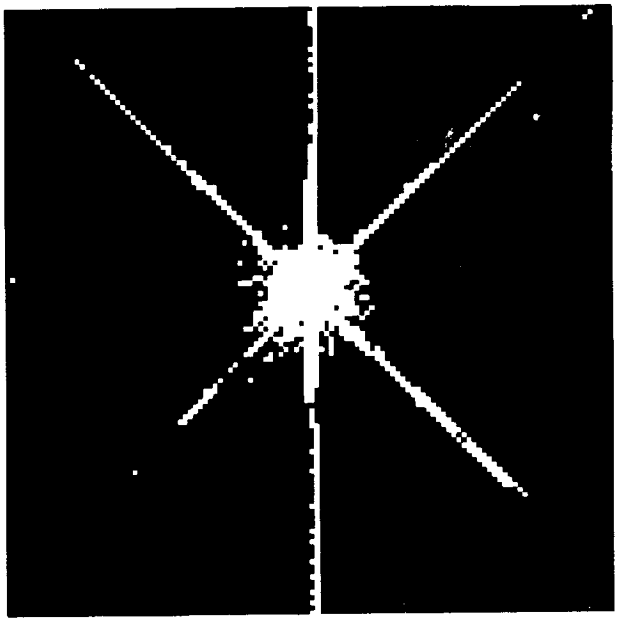

FIG. 13—Binary map resulting from the application of the modified search algorithm to the median F555W image shown in Fig. 1. The white elements identify those $5\times 5$ pixel arrays containing at least four pixels whose signals are at least $50\sigma$ above the local background. Clearly evident are the pupil diffraction spikes and the vertical charge bleed. The white elements surrounding the saturated core of the PSF are due to the highly variable radial streamers seen in Fig. 2. The white element at the extreme left center of the map is caused by a faint background star.

image are then examined directly to determine the cause of the brightness anomaly.

### 3.2 Algorithm Modifications

Three shortcomings of the basic search algorithm must be addressed before a satisfactory search for FCs can be undertaken. First, the brightness gradient across each $5\times 5$ pixel array caused by the radial decay of the PSF must be removed. Pixels closer to the center of the PSF generally will have larger signals than those farther from the center and thus may trigger FLAG=1 erroneously. To remove this gradient, we multiply the PC image by $\alpha^n$, where $n=3$ for $\alpha\lesssim 5''$ and $n=2$ for $\alpha\gtrsim 5''$ (see Sec. 2.3). Thus, step (3) becomes

(3) Compare $I\alpha^n$ for each pixel with $\langle I\alpha^n\rangle$ according to

$$\text{If } (I\ \alpha^n-\langle I\alpha^n\rangle)>N\langle\alpha^n\rangle\sigma,$$

$$\text{then FLAG}=1 \text{ else FLAG}=0.$$

Figure 12(a) is a surface plot of a noisy model F555W image containing a simulated companion located at $\alpha=4''$. The plot shows the $1''\times 1''$ region of the primary star's PSF centered on the companion. To produce the image, the PSF was first scaled to give a total signal of $10^{10}\,e^{-}$. A companion's signal was then divided uniformly over a $2\times 2$ pixel area so that each pixel was 10 $\sigma$ above the median background signal. Finally, a Gaussian distribution of noise was added to the image to mimic actual background fluctuations. Figure 12(b) shows the same image after removal of the brightness gradient. The companion is clearly more noticeable in the background-flattened image.

The second shortcoming of the basic algorithm appears when the anomalous pixels are sorted by $N$, the number of standard deviations from the local average signal. As written, the algorithm flags all pixels with signals exceeding $N\sigma$. To avoid duplicate identifications at successively smaller values of $N$, step 3 should be modified to flag those anomalous pixels whose signals lie in the range $N_1\sigma$–$N_2\sigma$.

Finally, the basic algorithm cannot discriminate between legitimate sources and fixed image artifacts (e.g., "hot" CCD pixels). Since FCs are likely to be imaged over a few contiguous pixels, step (3) should again be modified to flag only those arrays containing $m$ or more deviant pixels. Incorporating these last two modifications into step (3), we obtain

(3) Compare $I\ \alpha^n$ for each pixel with $\langle I\alpha^n\rangle$ according to

$$\text{If } N_1\langle\alpha^n\rangle\sigma<(I\ \alpha^n-\langle I\ \alpha^n\rangle)$$

$$<N_2\langle\alpha^n\rangle\sigma \text{ for } m \text{ or more pixels,}$$

$$\text{then FLAG}=1 \text{ else FLAG}=0.$$

### 3.3 Applying the Algorithm

We have applied the modified search algorithm to the median F555W image shown in Fig. 1. The binary map resulting from a search with $N_1=50$, $N_2=\infty$, and $m=4$ is shown in Fig. 13. Clearly evident in the map are the pupil diffraction spikes and the vertical charge bleed. The white

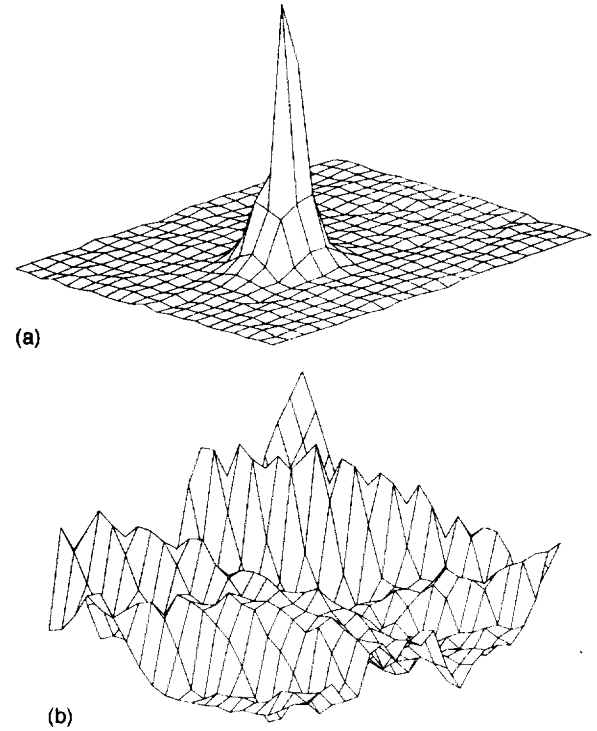

FIG. 14—Surface plots of 1″×1″ regions surrounding two brightness anomalies seen in Fig. 1. The anomalies were selected from the binary search map shown in Fig. 13. In each case, the local brightness gradient has been removed. (a) Surface plot of a faint background star identified by the white element seen at the extreme left center of the binary map. (b) Surface plot of a bright radial streamer identified by the white element seen to the upper left of the map's center.

elements surrounding the saturated core of the PSF are due to the highly variable radial streamers seen in Fig. 2. The white element at the extreme left center of the binary map is caused by a faint background star. Figures 14(a) and 14(b) show, respectively, surface plots of this background star and another brightness anomaly seen to the upper left of the map's center. In practice, we use surface plots or contour maps of regions displaying brightness anomalies to discriminate visually between possible FCs and uninteresting variations of the local PSF.

To test its effectiveness for detecting FCs, we have applied our search algorithm to noisy model images with a wide range of primary-to-companion brightness ratios and separations. We have found that the search algorithm will successfully find the simulated companions at all locations provided that the average pixel signal from the companion is at least $10\sigma$.

## 4. IMAGE SENSITIVITY AND STRATEGY

### 4.1 Detection Limits for Faint Companions

Because WFPC2 is not equipped with a coronagraphic mode, even short exposures of bright stars will saturate the detector. Thus, the strategy for imaging FCs must reflect a compromise between the desired point-source detection limit and lost circumstellar field of view. To assess the observational limits imposed by such a compromise, we adopt as a benchmark the Sun–Jupiter system projected to the distance of $\alpha$ Centauri A (1.3 pc). At this distance, Jupiter would appear ~4″ from the Sun and would have a magnitude of $V\approx 22$. The Sun itself would be as bright as $\alpha$ Cen A ($V=0$), so an imaging dynamic range of $\gtrsim 10^9$ would be required to detect the extrasolar Jupiter. We now investigate whether this dynamic range can be achieved within a reasonable time scale and without extensive saturation.

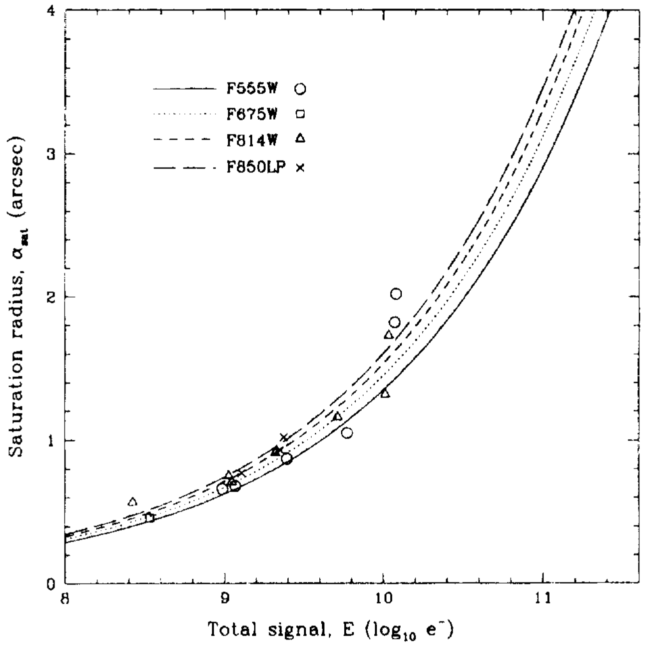

FIG. 15—Radius of PSF saturation, $\alpha_{\rm sat}$, as a function of total detected signal, $E$, for WFPC2 filters F555W, F675W, F814W, and F850LP. Using a detector gain of 14 $e^-$ DN$^{-1}$, saturation of the PC's A/D converter occurs when the bias-subtracted pixel signals reach $5.3\times10^4$ $e^-$. The curves have been scaled to provide a good visual fit to the ensemble of data obtained from actual PC images.

Equation (3) can be used to find the radius of saturation as a function of bandpass and total signal from the primary star. Using the larger gain option of 14 $e^-$ DN$^{-1}$, saturation of the PC's 12 bit analog-to-digital (A/D) converter occurs when the bias-subtracted pixel signals reach $5.3\times10^4$ $e^-$. Setting $\langle I\rangle$ equal to this value, we obtain

$$\alpha_{\rm sat}=0.5f\left[\frac{E}{10^9}\,\frac{\langle\lambda_{\rm nm}\rangle}{550}\right]^{1/3}\ \text{arcsec}, \tag{5}$$

where $\alpha_{\rm sat}$ is the radius of saturation, $E$ is the total signal in a single exposure, and $f$ is a scale factor that accounts for the brightness discrepancy between the PC and model PSFs (see Sec. 2.3). Equation (5) does not account for the effects of charge bleeding, so the resulting values of $\alpha_{\rm sat}$ should be considered approximate.

Figure 15 shows $\alpha_{\rm sat}$ vs. $E$ for the filters F555W, F675W, F814W, and F850LP with $f=3.15$. This scale factor produces a good visual fit to the ensemble of data obtained from actual PC images and shown in Fig. 15. In each case, our extrasolar Jupiter at $\alpha=4''$ would be obscured by PSF saturation if the total signal from the primary star reached $\sim 2\times10^{11}$ $e^-$. At this exposure level, the expected signal from the planet would be 200 $e^-$. Using Eq. (3) with the factor-of-3.15 brightness correction, we can compute the av-

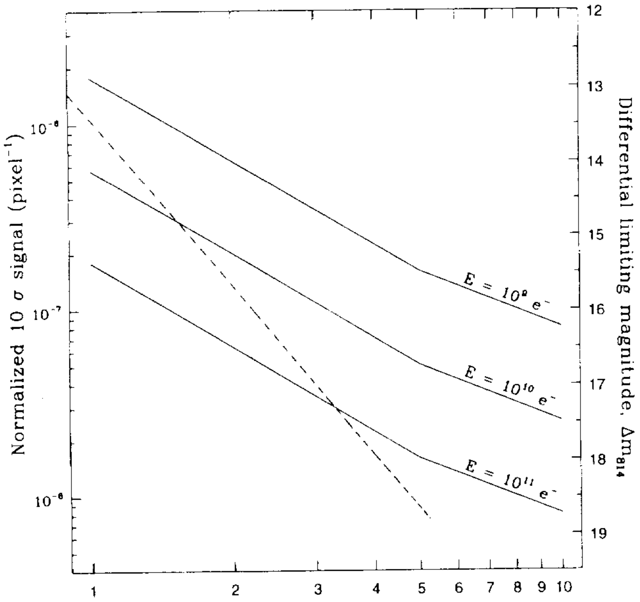

FIG. 16—$10\sigma$ detection limits for FCs imaged through F814W (WFPC2 $I$) at various primary-star exposure levels. Here, $\sigma$ is the square root (i.e., photon noise) of the PC's PSF shown in Fig. 10. The left scale measures the $10\sigma$ pixel signal as a fraction of the total signal, $E$, from the primary star. The right scale translates this signal into a differential magnitude, $\Delta m_{814}=m_{\rm FC}-m_{\rm star}$, assuming that the FC is imaged uniformly over four pixels, each of brightness $10\ \sigma$. The dashed line marks the radius of saturation shown in Fig. 15 for F814W. Detection limits to the right of this line can be achieved with a single image, while those to the left can be achieved only by summing multiple images of lesser exposure.

erage brightness of the PSF at $\alpha=4''$. For F555W ($\langle\lambda\rangle=540$ nm), we obtain $\langle I\rangle=7\times10^4\ e^-$. If the planetary signal were confined to one detector pixel, then the S/N per exposure of our extrasolar Jupiter would be 0.75. To achieve the $10\sigma$ limit necessary for guaranteed detection, 180 images would have to be obtained and summed. Given the present WFPC2 data-storage constraints, ten *HST* orbits would be required to record this number of images.

Our benchmark scenario shows that a comprehensive search for extrasolar Jovian planets with the PC is impractical at best. However, our analysis does not disprove the PC's usefulness for detecting FCs whose observable characteristics are unlike those of Jupiter. Figure 16 shows the $10\sigma$ detection limits for FCs plotted as a function of $\alpha$ for various primary-star exposure levels through F814W (WFPC2 $I$). Here, $\sigma$ is the square root (i.e., photon noise) of the PC's PSF shown in Fig. 10. The left scale in Fig. 16 measures the $10\sigma$ pixel signal as a fraction of the total signal from the primary star. The right scale translates this fractional signal into a differential magnitude, $\Delta m_{814}=m_{\rm FC}-m_{\rm star}$, assuming that the FC is imaged uniformly over four pixels, each of brightness $10\sigma$. As expected, $\Delta m_{814}$ increases as the exposure level increases. For a total signal of $10^9\ e^-$, our search algorithm will detect FCs that are 13 mag fainter than the primary star at $\alpha=1''$ and 15 mag fainter than the primary star at $\alpha=4''$. Dynamic-mass studies of the lower main sequence suggest that the substellar break occurs at $M_I\sim13$ (Kirkpatrick and McCarthy 1994). If so, we may detect brown dwarfs as faint as $M_I\sim16.7$ separated by $1''$ from $\alpha$ Cen A ($M_I=3.7$).

TABLE 1
Targets of Faint-Companion Search

| Name 1 | Name 2 | $d^a$ (pc) | $\mu^a$ ($''$ yr$^{-1}$) | $V^a$ | Spectral$^a$ Type | Category$^b$ |
|---|---|---|---|---|---|---|
| L 726-8 AB | Gl 65AB | 2.7 | 3.36 | 12.5+13.0 | M5.5Ve+M5.5Ve | NS,UV |
| HD 10700 | $\tau$ Cet | 3.6 | 1.92 | 3.5 | G8V | NS |
| HD 16160 | Gl 105A | 7.2 | 2.32 | 5.8 | K3V | AB |
| HD 22049 | $\epsilon$ Eri | 3.3 | 0.98 | 3.7 | K2V | NS |
| HD 48915A | Sirius | 2.7 | 1.33 | −1.5 | A1V | NS |
| HD 61421A | Procyon | 3.5 | 1.25 | 0.4 | F5V | NS |
| HD 90839 | 36 UMa A | 12.0 | 0.18 | 4.8 | F8V | AB |
| Wolf 359 | Gl 406 | 2.3 | 4.70 | 13.5 | M8e | NS,UV |
| L 145-141 | Gl 440 | 4.9 | 2.68 | 11.4 | | NS,WD |
| Ross 128 | Gl 447 | 3.3 | 1.38 | 11.1 | M5 | NS,UV |
| Proxima Cen | Gl 551 | 1.3 | 3.85 | 11.1 | M5e | NS,UV |
| HD 128620 | $\alpha$ Cen A | 1.3 | 3.68 | 0.0 | G2V | NS |
| HD 128621 | $\alpha$ Cen B | 1.3 | 3.68 | 1.3 | K0V | NS |
| BD +4°3561 | Barnard's | 1.8 | 10.34 | 9.5 | M5V | NS,AB |
| Ross 154 | Gl 729 | 2.9 | 0.72 | 10.6 | M4.5e | NS,UV |
| HD 187642 | Altair | 5.1 | 0.66 | 0.8 | A7V | NS |
| G 208-44/5 | GJ 1245AB | 4.7 | 0.74 | 13.4+14.0 | | NS,UV |
| Ross 248 | Gl 905 | 3.1 | 1.60 | 12.3 | M6e | NS,UV |

[a] From Gliese (1969) or Gliese & Jahreiss (1979).

[b] AB Astrometric Binary; NS Nearby Star ($d<5$ pc); UV Ultraviolet Flare Star; WD White Dwarf.

The dashed line in Fig. 16 marks the radius of saturation shown in Fig. 15 for F814W. Detection limits to the right of this line can be achieved with a single image, while those to the left can be achieved only by summing multiple images of lesser exposure. For summed images, the detection limits are valid only in those regions where the pixel signals are comfortably above the quantization floor of the detector. This floor is governed by the A/D gain and the CCD read noise. For our purposes, the A/D gain is 14 $e^-$ DN$^{-1}$ and the read noise is 7 $e^-$ (Burrows et al. 1995). The faintest detectable object is that which is sufficiently luminous to produce one DN (in our case, a signal of 7–21 $e^-$). The magnitude of this object can be increased only by lengthening the exposure time. It cannot be increased by summing multiple images of a given exposure time.

### 4.2 Observing Strategy

The 18 target stars of our search program are listed in Table I. While composing our observing strategy, we have made no *a priori* assumptions about the nature or location of possible FCs unless, as in the case of the astrometric binaries, existing literature constrains the search space. We have adopted an inner limit of $0\farcs5<\alpha<1''$ for searching the circumstellar environments of our targets. Thus, we determine the exposures of each target star based on a detected signal per exposure of $10^8$–$10^9\ e^-$ (see Fig. 15).

Identification of actual FCs is contingent upon common proper motion between the target star and its FC candidate. This test for companionship requires two *HST* visits to the target separated by enough time to allow an unambiguous detection of motion. To ensure that the target's motion exceeds the uncertainty of its saturated-image centroid ($\lesssim0.5$ pixel), we require that the target's motion between visits be at least 5 pixels. Because the annual proper motions of our targets are large, the two visits often can be scheduled within a few weeks of each other. Such scheduling permits the use of the same guide stars for each visit, which guarantees duplicate pointings and reproducible PSFs. To expose any FCs potentially obscured by the charge bleed or diffraction spikes, a second set of visits with a 10°–15° roll offset is scheduled when possible.

During the first visit to each target, several exposures are recorded through two broadband filters to provide two-color photometry of any field objects. Typically, we use F555W (or F675W) and F814W because they provide a long-wavelength baseline over which very red objects, like brown dwarfs, may be easily identified. During the second visit, an identical set of exposures through F814W is recorded. Using broadband filters ensures that the target's PSF is free of interference fringes within the angular range of interest ($\lesssim 10''$). Our original plan to search for FCs within the interference minima of narrow-band images was aborted because the unfavorable response function of the CCD pixels (Burrows et al. 1995) significantly reduces fringe contrast.

Observations of our target stars are presently underway. The results of these observations are beyond the scope of this paper and will be published elsewhere. The first *HST* images of the very-low-mass companion to the astrometric binary Gl 105A have already been reported (Golimowski et al. 1995). A long-term program to monitor the orbital motion of the companion with *HST* is planned.

## 5. CONCLUSIONS

A search for faint companions (FCs) to selected stars within 5 pc of the Sun using the *Hubble Space Telescope*'s Planetary Camera (PC) has been initiated. To assess the PC's ability to detect FCs, we have constructed both model and laboratory-simulated PSFs and compared them to actual PC images. We find that the PC's PSF in the angular range $2'' < \alpha \lesssim 5''$ is 3–4 times brighter than expected with a perfect detector and optics, but the surface brightness retains the $\alpha^{-3}$ dependence characteristic of a perfect PSF. For $\alpha \gtrsim 5''$, the radial dependence changes to $\alpha^{-2}$. We conclude that zonal figure errors in *HST*'s mirrors are at least partly responsible for the enhanced brightness within 5″. The azimuthal variations of the PC's PSF are 10–20 times larger than expected for a perfect PSF, but are consistent with those of the laboratory-simulated images obtained with a flight-spare CCD. These variations suggest that light is scattered radially but nonuniformly from the surface of the CCD.

The anomalies seen in the PC's PSF are field dependent and unreproducible by modeling or laboratory simulation. Therefore, subtracting a reference PSF from the image is problematic. Consequently, we have developed a computer algorithm that identifies local brightness anomalies within the PSF as potential FCs. We have applied this search algorithm to noisy model images of binary systems with varying separations and brightness ratios. We find that the search algorithm successfully finds the simulated companions at all locations provided that the average pixel signal from the companion is at least $10\sigma$ above the local background.

Adopting the $10\sigma$ minimum as our FC detection limit, we determine that at least ten orbits of *HST* observing time would be required to detect a Jupiter-like planet lying 4″ from $\alpha$ Cen A. Although a comprehensive search for extrasolar Jovian planets would be impractical, the PC is useful for imaging other types of substellar objects. We have translated the $10\sigma$ signal limit to a differential-magnitude detection limit in the WFPC2 $I$ bandpass. As expected, this differential-magnitude limit increases as the exposure level increases. For a total detected signal of $10^9\ e^-$, our search algorithm is capable of detecting FCs that are 13 mag fainter than the primary star at $\alpha = 1''$ and 15 mag fainter than the primary star at $\alpha = 4''$. These limits imply that we may detect brown dwarfs as faint as $M_I = 16.7$ separated by 1″ from $\alpha$ Cen A. A tenfold increase in the exposure level increases this limiting magnitude by 1.25.

William G. Fastie, Research Professor at The Johns Hopkins University, proposed this faint-companion search program about 1980 and has been the driving force behind it. D.J.S. has been privileged to work with Professor Fastie both as a co-member of the Space Telescope Science Working Group and as a co-principal investigator of this search program. The authors are also grateful to James Westphal and John Trauger for their cooperation and assistance with the construction of SIM. We thank Christopher Burrows and John Krist for many useful discussions regarding WFPC2 performance. Finally, we thank Alexandra Cha and Richard Zubrowski for their assistance in the laboratory. This research has been supported by NASA Grants No. NAG 5-1620 (D.J.S.) and No. NAG 5-1617 (W. G. Fastie, PI).

## REFERENCES

Brown, R. A., and Burrows, C. J. 1990, Icarus, 87, 484

Burrows, C. J., Baggett, S. M., Biretta, J., Casertano, S., Clampin, M., Griffiths, R. E., and Krist, J. 1995, WFPC2 Instrument Handbook Version 3.0 (Baltimore, STScI)

Fastie, W. G., Schroeder, D. J., Harrington, R. S., and Henry, R. C. 1985, A Photometric Search for Planets of Nearby Stars, NAS 5-29259 (Washington, NASA)

Gliese, W. 1969, Catalogue of Nearby Stars, Veroff. Astron. Rechen.-Inst. Heidelberg, No. 22

Gliese, W., and Jahreiss, H. 1979, A&AS, 38, 423

Golimowski, D. A., Fastie, W. G., Schroeder, D. J., and Uomoto, A. 1995, ApJ, 452, L125

Hasan, H. 1994, Instrument Science Report No. OTA 17 (Baltimore, STScI)

Kirkpartick, J. D., and McCarthy, D. W., Jr. 1994, AJ, 107, 333

Krist, J. 1994, The Tiny Tim User's Manual Version 4.0 (Baltimore, STScI)

Krist, J. E. 1995, in Calibrating *Hubble Space Telescope:* Post-Servicing Mission, ed. A. Koratkar and C. Leitherer (Baltimore, STScI), p. 311

Krist, J. E., and Burrows, C. J. 1995, Appl. Opt., 34, 4951

Schroeder, D. J. 1987, Astronomical Optics (San Diego, Academic)